Hybrid Analytical Model of Permanent Magnet Linear Motor Considering Iron Saturation and End Effect

Zhaokai Li, *Member, IEEE*, Lize Wu, *Graduate Student Member, IEEE*, Yanxin Li, *Member, IEEE*, Qinfen Lu, *Senior Member, IEEE*, Xiaoyan Huang, *Member, IEEE*, Luca Peretti, *Senior Member, IEEE*, and Yiming Shen, *Member, IEEE*

***Abstract*—This paper proposed a hybrid analytical model for predicting the magnetic field distribution of slotted surface-mounted permanent magnet linear motor considering both iron saturation and end effect. In the proposed model, the segmented conformal mapping is developed to reduce the computation time while keeping same accuracy, especially when the end effect significantly affects the motor performance. Then, with the help of the magnetic circuit model in the primary and secondary iron, the magnetic potential drop of iron is obtained from the iterative calculation. The equivalent saturation current is introduced to represent the iron saturation and finally the performance of permanent magnet linear motor can be obtained considering both iron saturation and end effect. The proposed model expands the scope of the analytical models for the analysis of linear motors. The finite element analysis and experimental validation are carried out to show the effectiveness of the proposed model.**

***Index Terms*—Hybrid analytical model, permanent magnet linear motor, iron saturation, end effect.**

I. Introduction

LINEAR motors show great advantages over rotary motors in converting into linear and reciprocating motions due to their compact structure and easy maintenance. Hence, they have been widely used in magnetic levitating trains, robotic arms, and semiconductor manufacturing equipment [1], [2], [3]. Before investigating the characteristic of linear motors, one could always use the information from the corresponding rotary motor first, as both linear and rotary motors are designed based on the same principle. Nevertheless, some unique features can only be observed in linear motors, such as longitudinal end effect and special cooling conditions, which makes the analysis and design of linear motors 'special'.

The optimal design of the linear motor is paramount for maximizing performances and requires an accurate electromagnetic model. Three methods are widely used to predict linear motor performance, i.e., finite-element method (FEM), analytical models, and magnetic circuit models (MCM). FEM takes advantage of high calculation accuracy for different types of linear motors, but suffers from large computational burden [4]. A long primary and long secondary linear motor were investigated to increase the thrust force density by using FEM in [5], [6], [7]. However, the long primary or secondary in the linear motor can significantly increase the calculation time of the magnetic field and there is no periodic boundary condition at the longitudinal ends, making the design and optimization of the linear motors more time-consuming.

Most of the analytical models assume the infinitely permeable iron in the permanent magnet linear motor (PMLM) and only focus on the calculation of the magnetic field in the region with vacuum permeability. In [8], the analytical calculation of the slotless PMLM was introduced to predict the open-circuit and armature magnetic field in the air-gap for different magnetization patterns. Then, the slotting effect was considered using the complex permeance function from conformal mapping in [9], and the end effect was simplified using virtual slots at both primary ends. However, this approach introduces large errors if the slot-opening of the virtual slot is large compared to the virtual tooth width. Meanwhile, Schwarz-Christoffel (SC) mapping was another form of conformal mapping to transform the slotted air-gap region into the slotless region, and the linear analytical solution of the PMLM performance was obtained in [10], [11], [12]. However, it is observed that the inverse SC mapping occupied most of the calculation time, which should be optimized to guarantee high computational efficiency [11]. This is also one of the focus areas in this paper.

Manuscript received 6 September 2023; revised 12 December 2023; accepted 28 December 2023. Date of publication 16 January 2024; date of current version 22 August 2024. This work was supported in part by the National Natural Science Foundation of China under Grants 52107060 and 52177061, and in part by the Zhejiang Provincial Natural Science Foundation of China under Grant LQ22E070003. Paper no. TEC-01024-2023. *(Corresponding author: Yiming Shen.)*

Zhaokai Li and Luca Peretti are with the Division of Electric Power and Energy Systems, KTH Royal Institute of Technology, SE-10044 Stockholm, Sweden (e-mail: zhaokai@kth.se; lucap@kth.se).

Lize Wu, Yanxin Li, Qinfen Lu, and Xiaoyan Huang are with the College of Electrical Engineering, Zhejiang University, Hangzhou 310027, China (e-mail: wulize@zju.edu.cn; eeliyanxin@zju.edu.cn; luqinfen@zju.edu.cn; xiaoyanhuang@zju.edu.cn).

Yiming Shen is with the School of Electrical and Electronic Engineering, Nanyang Technological University, Singapore 639798 (e-mail: yiming.shen@ntu.edu.sg).

Color versions of one or more figures in this article are available at https://doi.org/10.1109/TEC.2024.3354488.

Digital Object Identifier 10.1109/TEC.2024.3354488

Another category of analytical models is based on the method of separation of variables to account for the slotting effect. It solves the coefficients of the general analytical model using the boundary and interface conditions. In [13], it was modified by transforming the PMLM into an arc-linear PMSM to predict cogging force. Then the work was directly conducted in Cartesian coordinates combined with the periodic extension method for PMLM in [14]. For the linear motor with short moving-magnet, the virtual regions were used to consider the end effect in [15]. However, these methods in [13], [14], [15] are only validated for PMLM under open-circuit conditions when the iron saturation is insignificant. Furthermore, the iron region could be divided into small subdomains according to the finite iron permeability, and then the method of separation of variables was employed to predict the magnetic field in these subdomains [16], [17]. These models exhibit improved accuracy in predicting the performance of rotary permanent magnet motors due to considering iron saturation, but they are not suitable for linear motors.

As these analytical models in [8], [9], [10], [11], [12], [13], [14], [15] cannot consider the iron saturation, MCM can be used to make up for this shortcoming. In [11], the MCM was compared with an analytical model and they all had good accuracy in calculating thrust force. In [18], some representative parameters of MCM were extracted from a small number of FEM results and then the large design space of PMLM could be explored using MCM. In [19], the general mesh method was employed to obtain the MCM with dense reluctance, and therefore it was feasible to predict the complex air-gap flux density in the linear PM vernier motor. However, there is a trade-off between the calculation speed and accuracy for MCM when establishing different sizes of the magnetic circuit for the same linear motor, especially for the air-gap region with irregular flux distribution. Hence, the hybrid analytical model was proposed to scale down the MCM while keeping high accuracy. In [20], the magnetic field in the air-gap and PM region was predicted using analytical model, while the slot and iron region were built using the MCM. This method saves time for calculating the complex flux distribution in the air-gap, but it still requires large computation in the analysis of slot leakage and end effect using the MCM. In fact, the combination of analytical model and MCM has been investigated in the rotary PM motors such as surface-mounted PM motors [21], [22], [23], IPM motors [24], [25], [26], and vernier PM motors [27], but there is a lack of application for PMLMs, which is the contribution of this paper.

This paper focuses on the hybrid analytical model (HAM) to predict the magnetic field distribution of the PMLM with high accuracy. Compared with FEM, the HAM can significantly reduce the calculation, which is useful for the initial motor design. It combines the segmented conformal model (SCM) and MCM considering both iron saturation and longitudinal end effect. In Section II, the SCM is developed to calculate the air-gap field in the middle region and the end region separately to improve the calculation speed while keeping the same accuracy. Then, in Section IV, the modified MCM is introduced to include the air-gap flux produced by winding current, PM, and the equivalent saturation current. After building the relationship between the equivalent saturation current and the nonlinear magnetic potential of iron, the solving loop is obtained to predict the convergent iron permeability in the modified MCM. Hence, the HAM further improves the prediction accuracy of the PMLM performance by adding the magnetic field produced by the equivalent saturation current in the analytical solution. In Section V, both FEM and experiment of the PMLM are carried out to verify the effectiveness of the proposed model.

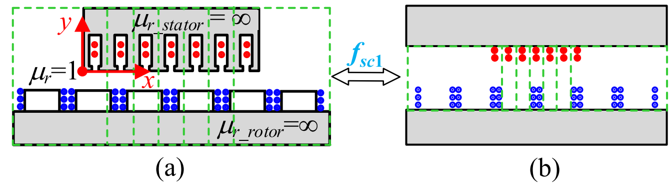

Fig. 1. Conformal mapping between (a) the whole slotted domain and (b) the whole slotless rectangular domain.

II. Segmented Conformal Model

Unlike rotary motors that always follow the principle of periodic field, the linear motor exhibits significant flux leakage at the longitudinal end of the motor, leading to inaccurate prediction of air-gap field based on the conventional analytical models [8]. Therefore, the SCM is firstly introduced based on the modified periodicity to accurately account for the end effect of PMLM while reducing the computational burden of the proposed method. The following assumptions are made for SCM:

1) The transversal end effect is neglected.
2) The eddy current reaction is neglected.
3) The relative permeability of the magnet is equal to 1.
4) The iron permeability is infinite.

A. Conformal Mapping

SC mapping will transform the slotted domain into the rectangular domain [10], [28]. The analytical expression of the magnetic field can be directly obtained in this rectangular domain. As the inverse of the SC mapping is conformal, the magnetic field solution in the original slotted domain can be derived from that in the rectangular domain. Based on this theory, the SC mapping is employed to build the relationship between the slotted domain of PMLM and the slotless rectangular domain, as shown in Fig. 1 [10], [28].

$$Z = f_{SC}(W) = A_0 \int \prod_{k=1}^{n-1} (W - w_k)^{-\frac{\beta_k}{\pi}} dW + C_0 \tag{1}$$

where Z and W are the corresponding positions using the complex numbers in the slotted and slotless domain, respectively. A_0, C_0, ω_k, and β_k are the SC parameters. They are calculated according to the dimension of the slotted domain including air-gap, PM, and slot region, as they have the same permeability. However, transforming the whole slotted domain into the slotless domain is time-consuming when the slot number of PMLM becomes large.

To avoid this situation, the slotted domain of PMLM is divided into two categories, i.e., the single end-slot domain and the single

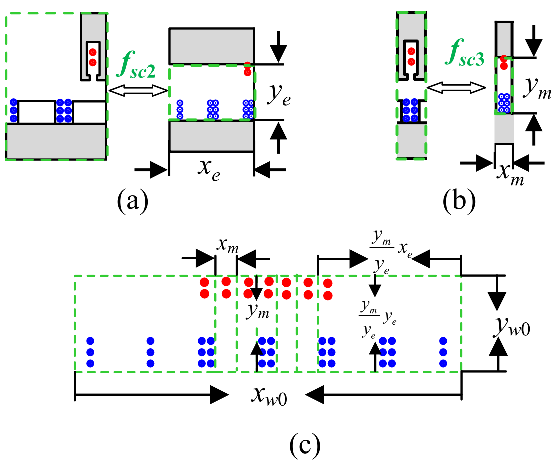

Fig. 2. Transformation based on the segmented conformal mapping. (a) SC mapping for the single end-slot domain. (b) SC mapping for the single mid-slot domain. (c) The whole slotless rectangular domain.

mid-slot domain, according to the modified periodicity. The slot domains at two ends of PMLM (the end-slot single domain) are responsible for the end effect and the same SC mapping can be used to obtain the slotless rectangular domains corresponding to the end regions, as shown in Fig. 2(a). Similarly, other slot domains in between exhibit the same shape and they can all be mapped separately based on the other SC mapping, as shown in Fig. 2(b). Therefore, only two SC mappings are required with significantly reduced computation. It is noted that the heights of the single end-slot domain and the single mid-slot domain are usually different. The following conformal mapping is used to normalize the geometry of these slotless domains.

$$\begin{cases} x_{w0} = \frac{2y_m x_e}{y_e} + (Q_s - 1)x_m \\ y_{w0} = y_m \end{cases} \tag{2}$$

where Q_s is the slot number of PMLM.x_{w0}, y_{w0}, x_e, y_e, x_m, and y_m are the width and height of the rectangles for the whole domain, single end-slot domain, and single mid-slot domain, respectively. They are also defined in Fig. 2. When the heights of these two kinds of slotless rectangular domains become the same using (2), these slotless rectangular domains in Fig. 2(a) and (b) can be horizontally arranged to form the entire slotless domain in Fig. 2(c). Such simplification neglects the mutual influence between the end slot domain and the middle domain during SC mapping. However, only slight differences are observed, which is demonstrated in this paper. Besides, the mutual relationship of the magnetic field between the end slot domain and the middle domain still exists, which will be shown in the next subsection.

B. General Solution

The total magnetic vector potential A_{zt} in the air-gap of the PMLM is calculated based on the superposition principle when neglecting iron saturation.

$$A_{zt}(z_p) = \sum_{k=1}^{N_{PM}+N_w} A_{zik}(z_p(x_p, y_p), z_i(x_{ik}, y_{ik}), i_k) \tag{3}$$

where N_{PM} and N_w are the number of PM equivalent current and winding current. $N_w = Q_s + 1$. A_{zki} represents the magnetic vector potential at the air-gap position z_p in the complex plane, which is produced by the equivalent current i_k at the position z_i. It is noted that $z_p = x_p + i * y_p$ and $z_i = x_i + i * y_i$. The equivalent current will be replaced by the actual value and position of the PM equivalent current and winding current in the analytical calculation. Then, based on the segmented conformal mapping, z_p and z_i in the whole slotted domain can be conformally transformed to w_p and w_i in the whole slotless domain, respectively.

$$z(x_z, y_z) = g_0(w(x_w, y_w)) = \begin{cases} f_{sc3}(w(x_w, y_w)), l_{sl} \le x_z \le l_{st} - l_{sl} \\ f_{sc2}(\frac{y_m}{y_e} w(x_w, y_w)), \text{otherwise} \end{cases} \tag{4}$$

where Fig. 1(a) gives the rectangular coordinate system for the whole slotted domain. $z = x_z + i * y_z$ and $w = x_w + i * y_w$. l_{st} is the total length of the primary iron and l_{sl} is the slot-pitch. $\{z_p, z_i\} \subset z$ and $\{w_p, w_i\} \subset w$. As the magnetic ector potential keeps the same in the conformal mapping, the magnetic vector potential A_z can be obtained using the following equation [29].

$$\begin{aligned} &A_{zik}(z_p, z_i, i_k) = A_{zik}(w_p, w_i, i_k) \\ &= \frac{\mu_0 i_k}{2\pi}\Bigg\{\ln|w_p - w_i| - \sum_{k=1}^{+\infty}\Big[\cosh(2\pi k(y_{wp} - y_{w0})/x_{w0}) \\ &\quad + e^{2\pi k(2y_{wi} - y_{w0})/x_{w0}}\cosh(2\pi k y_{wp}/x_{w0})\Big] \\ &\frac{e^{-2\pi k y_{wi}/x_{w0}}}{k\sinh(2\pi k y_{w0}/x_{w0})}\cos(2\pi k(x_{wp} - x_{wi})/x_{w0})\Bigg\} \end{aligned} \tag{5}$$

The x and y components of the total air-gap flux density in the slotted domain can be derived from $A_{zt}(z_p)$ using [24]

$$B_x(z_p) = \frac{\partial A_{zt}(w_p)}{\partial y_{wp}}\lambda_x(w_p) - \frac{\partial A_{zt}(w_p)}{\partial x_{wp}}\lambda_y(w_p) \tag{6}$$

$$B_y(z_p) = -\frac{\partial A_{zt}(w_p)}{\partial x_{wp}}\lambda_x(w_p) - \frac{\partial A_{zt}(w_p)}{\partial y_{wp}}\lambda_y(w_p) \tag{7}$$

where $\frac{\partial A_{zt}(w_p)}{\partial y_{wp}}$ and $\frac{\partial A_{zt}(w_p)}{\partial x_{wp}}$ can be analytically obtained from (5). The complex permeance λ is derived from the conformal mapping function (4).

$$\lambda = \lambda_x(w_p) - j * \lambda_y(w_p) = \frac{1}{g_0'(w_p)} \tag{8}$$

where $\lambda_x(w_p)$ and $\lambda_y(w_p)$ is the real and imaginary part of the complex permeance λ, respectively.

III. Modified Magnetic Circuit of Iron

To account for the iron saturation, the magnetic circuit of iron is built and exported to the SCM. Meanwhile, the magnetic field prediction in the whole slotted domain using SCM will help to simplify the structure of the MCM while keeping high accuracy.

Fig. 3 shows the modified MCM to represent the primary and secondary iron of the PMLM. The fluxes flowing into the primary and secondary iron are represented using the flux

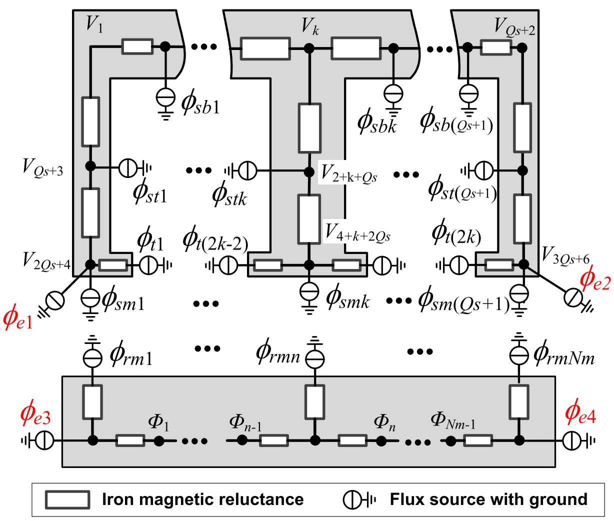

Fig. 3. Modified magnetic circuit model of iron.

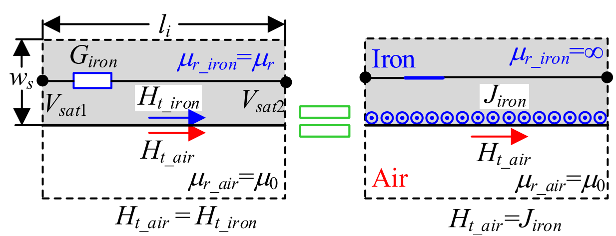

Fig. 4. Transformation of iron saturation using the equivalent current in the analytical solution.

sources with the ground rather than the magnetic reluctances in the air-gap, slot, and PM [24]. They are produced by the winding current and PMs while their value can be directly obtained based on the segmented conformal mapping. The primary and secondary iron with regular shapes can be represented using the magnetic reluctances in either x or y direction and their values are expressed as: [30]

$$G_{iron} = \frac{\mu_r l_{tr} w_s}{l_i} \tag{9}$$

where l_{tr} is the transversal length of PMLM. w_s and l_i are the width and length of rectangular iron, respectively. They are also defined in Fig. 4. μ_r is the iron permeability.

Then, the general expression of the magnetic potential matrix $\boldsymbol{V}$ in the iron can be expressed as [30]

$$f(\mathbf{V}) = \mathbf{A_{sr}} \mathbf{\Lambda_{sr}} \mathbf{A_{sr}}^{\mathbf{T}} \mathbf{V} - \mathbf{\Phi_z} = \mathbf{0} \tag{10}$$

where $\boldsymbol{V} = [V_1, \ldots, V_{3Q_s+6}, \Phi_1, \ldots, \Phi_{N_m+1}]^T$ in Fig. 3. $\mathbf{A_{sr}}$ is incidence matrix that is derived from Fig. 3. $\boldsymbol{\Lambda_{sr}}$ is the matrix of iron reluctance from (9) and Fig. 3. $\mathbf{\Phi_z}$ is the matrix of flux from the slotted domain, but it is noted that iron saturation is not considered at this step. According to Fig. 3, $\mathbf{\Phi_z}$ consists of $\phi_{sbk}, \phi_{stk}, \phi_{tk}, \phi_{smk}, \phi_{rmk}, \phi_{ek}$. These elements in $\boldsymbol{\Phi_z}$ can be calculated using [29]

$$\phi_i = l_{tr}[A_{zt}(z_{p1}) - A_{zt}(z_{p2})] \tag{11}$$

where z_{p1} and z_{p2} are the boundaries for calculating flux.

IV. Hybrid Analytical Model

A. Field-Circuit Coupling

The process of field-circuit coupling is a significant step to consider the iron saturation in the SCM. According to (11), the analytical solution of the slotted domain (air-gap, PM, and slots) is transferred to the flux source in the modified magnetic circuit model. Hence, it is obvious to focus on how to exhibit the influence of the iron magnetic potential on the magnetic field of the slotted domain in the PMLM. As the magnetic field strength in the tangential direction between the iron and the slotted domain remains continuous due to the absence of surface current density, it is feasible that the surface current is introduced to replace the tangential magnetic field strength of iron, as shown in Fig. 4. Therefore, the equivalent saturation current i_{sat} is expressed as [24]

$$i_{sat} = J_{iron} l_i = H_{t\_iron} l_i = V_{sat1} - V_{sat2} \tag{12}$$

where J_{iron} and H_{t_iron} are the equivalent saturation current density and tangential magnetic field strength. V_{sat1} and V_{sat2} are the magnetic potentials of the iron reluctance near the boundary. The equivalent saturation current is located near the boundary between the iron and the slotted domain. Finally, the total magnetic vector potential A_{zt} is derived from (3)

$$A_{zt}(z_p) = \sum_{k,i=1}^{N_{PM}+N_w+N_{iron}} A_{zik}(z_p, z_i, i_k) \tag{13}$$

where N_{iron} is the number of equivalent saturation current. Accordingly, the calculation of the magnetic field in the PMLM should be updated via the new A_{zt} considering iron saturation. Similarly, the flux linkage and back EMF of PMLM is calculated using [24]

$$\Psi_{ph} = N_0 \sum_{n_1,n_2} l_{tr} \left[A_{zt}(z_{pn_1}) - A_{zt}(z_{pn_2})\right] \tag{14}$$

$$U_{ph} = \frac{d\Psi_{ph}}{dt} \tag{15}$$

where N_0 is the number of coil turn. z_{pn_1} and z_{pn_2} are the central position of the slot.

The thrust force and normal force of the PMLM are calculated using [31]

$$F_x = \frac{l_{tr}}{\mu_0} \int_{l_{s1}}^{l_{s2}} B_x(z_{px}) B_y(z_{px}) dx \tag{16}$$

$$F_y = \frac{l_{tr}}{2\mu_0} \int_{l_{s1}}^{l_{s2}} \left[{B_x}^2(z_{px}) - {B_y}^2(z_{px})\right] dx \tag{17}$$

where l_{s1} and l_{s2} are the boundaries of the PMLM in the longitudinal direction. z_{px} is the position in the middle of the air-gap along the longitudinal direction.

B. Solving Process

Compared with SCM using (3), HAM using (13) incorporates the analytical solution of the magnetic field produced by the equivalent saturation current to exhibit higher accuracy. To obtain the nonlinear value of the equivalent saturation current, the

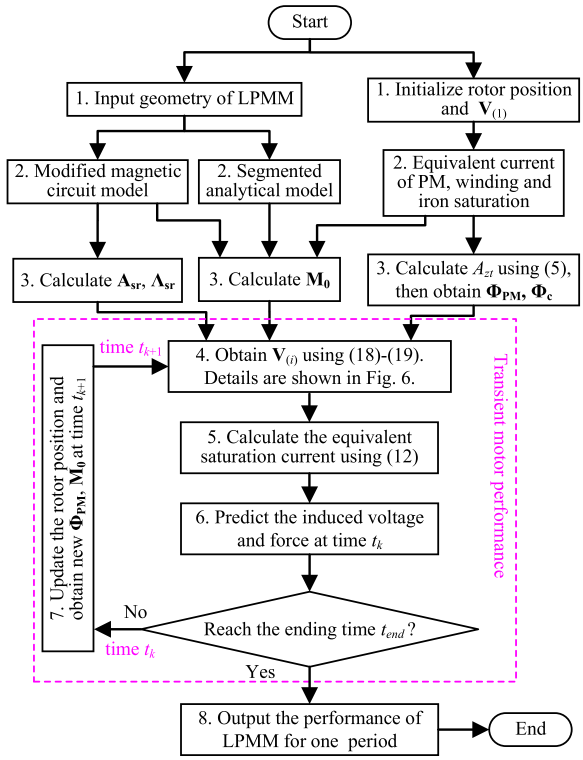

Fig. 5. Solving process of HAM.

modified MCM using (10) is proposed to iteratively determine the saturation level of the primary and secondary iron. Therefore, the flux source matrix Φ_z in (10) should be updated to include the flux produced by the equivalent saturation current using (11) and (13). To employ Newton's method in this loop, the following equation is derived from (10), (11), and (13).

$$f(\mathbf{V}) = \mathbf{A_{sr}}\mathbf{\Lambda_{sr}}\mathbf{A_{sr}}^{\mathbf{T}}\mathbf{V} - \mathbf{\Phi_{PM}} - \mathbf{\Phi_c} - \mathbf{M_0}\mathbf{V} = \mathbf{0} \quad (18)$$

$$\mathbf{V}_{(i+1)} = \mathbf{V}_{(i)} - r_{(i)} f(\mathbf{V}_{(i)})\left(\mathbf{A_{sr}}\mathbf{\Lambda_{sr}}\mathbf{A_{sr}}^{\mathbf{T}} - \mathbf{M_0}\right)^{-1} \quad (19)$$

where $\mathbf{\Phi_{PM}}$ and $\mathbf{\Phi_c}$ are the flux produced by the PM equivalent current and winding current using (11), respectively. $\mathbf{M_0}$ is the constant matrix from (11)–(13). $\mathbf{V}_{(i+1)}$ and $\mathbf{V}_{(i)}$ represent the solution of magnetic potential in the iron at the $(i+1)$th and ith step. $r_{(i)}$ is the relaxation factor at the ith step. The general solving process based on HAM is shown Fig. 5.

In the PMLM, it is difficult to obtain the convergent value of $\mathbf{V}$ due to the large flux leakage at the primary ends. This paper introduces the modified relaxation factor to obtain the convergent solution of $\mathbf{V}$. Usually, the range of $r_{(i)}$ is constant between 0.4 and 0.9 to reach convergence with good speed in the iteration. However, when it gets out of the solving loop with no convergence, the solution of $\mathbf{V}$ will produce the wrong magnetic field, which is not considered in most hybrid analytical models [21], [32]. Fig. 6 shows the flowchart for calculating $\mathbf{V}$ in Newton's method. It is found that the proposed method always gives a satisfactory and convergent solution for HAM as long as the longitudinal end flux ϕ_{ek} is accurately predicted. The large relaxation factor helps to save the time of the iterative

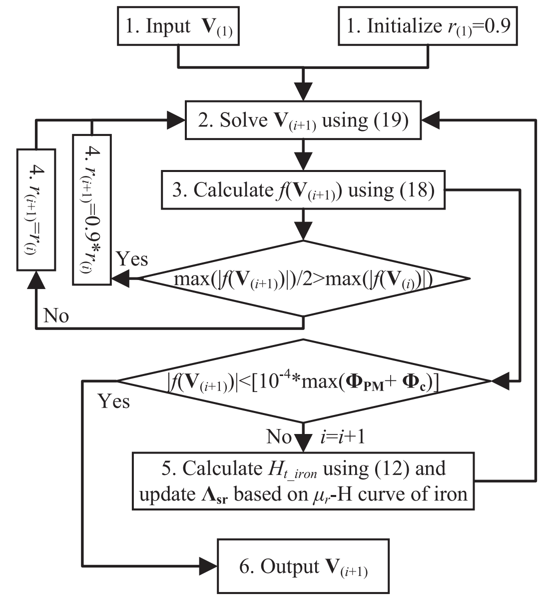

Fig. 6. Flowchart for calculating **V**.

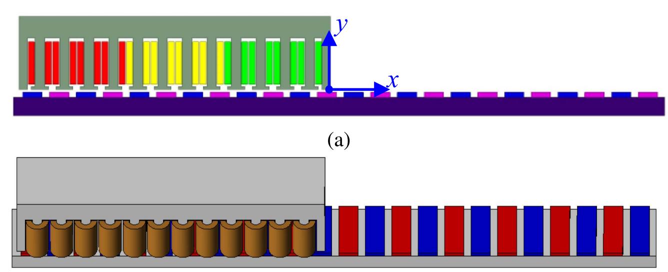

Fig. 7. FEM models of PMLM. (a) 2-D model. (b) 3-D model.

calculation at the beginning. As $|\ f(\mathbf{V}_{(i+1)})\ |$ becomes small, the iteration easily converges with the smaller value of relaxation factor, especially when the matrix $[\mathbf{A_{sr}}\mathbf{\Lambda_{sr}}\mathbf{A_{sr}}^{\mathbf{T}} - \mathbf{M_0}]$ is ill-conditioned.

V. FE and Experiment

The 2-D FEM was employed to verify the effectiveness of the SCM, as the proposed analytical model is 2-D. The 2-D view of the PMLM structure at the initial position is shown in Fig. 7(a). Meanwhile, the 3-D FEM is carried out and compared with the experimental results to demonstrate the high accuracy of the SCM, as shown in Fig. 7(b). Table I shows the values of the main parameters. The BH curves of primary and secondary iron are displayed in Fig. 8 and the flux density in the primary iron of the PMLM can be larger than 1.8 T at maximum load, which is severely saturated. SCM, HAM, and FEM with either nonlinearly or infinitely permeable iron are used to calculate the performance of the PMLM, including the magnetic field, flux linkage, induced voltage, and force.

The experiment of the PMLM prototype is carried out to verify the effectiveness of the proposed method, as shown in

TABLE I
MAIN PARAMETERS OF THE PMLM

Parameter	Value	Parameter	Value
primary iron length l_p	256 mm	primary iron height h_p	60 mm
secondary iron length l_s	484 mm	secondary iron height h_s	15 mm
pole pitch τ_m	22 mm	PM height h_{PM}	4 mm
PM width w_{PM}	16 mm	total pole number p_t	24
air-gap length l_{air}	2.5 mm	number of coil turn N_0	210
transversal length l_{tr}	50 mm	slot number Q_s	12
slot width w_{sw}	12.2 mm	slot height h_{slot}	40 mm
slot opening w_{so}	6.2 mm	tooth tip height h_{tt}	2.2 mm
middle tooth width w_{mt}	8 mm	end tooth width w_{et}	7 mm
extended end length l_{ee}	39 mm	end PM offset d_m	7.5 mm
PM remanence B_r	1.25 T	Nominal voltage U_n	48 V
Nominal power P_n	1.0 kW	Nominal efficiency η_n	0.90
Nominal current I_n	3.0 A	Nominal force F_n	243 N
Peak current I_{max}	6.0 A	Peak force F_{max}	441 N

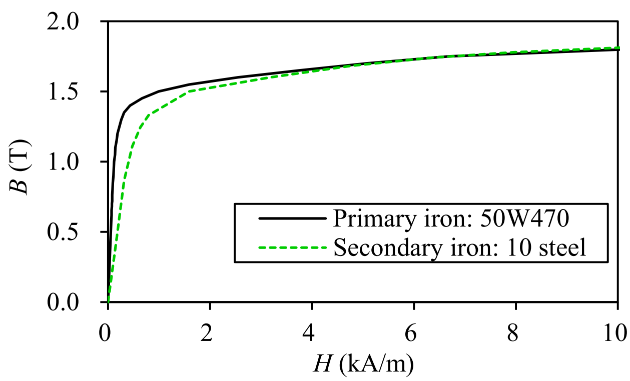

Fig. 8. BH curves of the primary and secondary iron.

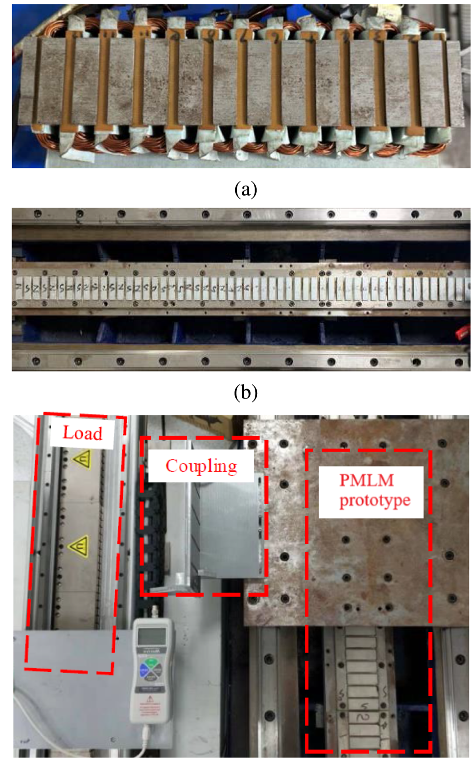

(a)

(b)

(c)

Fig. 9. Prototype and experimental test bench of PMLM. (a) The primary. (b) The secondary. (c) Test bench.

Fig. 9. The primary is mounted on a mover guided by two linear guides, while the secondary is positioned on the stator between two linear guides. The test bench in Fig. 9(c) comprises two components: a prototype platform and an air-core PMLM. These two components are coupled through a force meter capable of recording real-time acting force. During open circuit performance tests, such as back-EMF and detent force evaluations, the air-core PMLM is driven by an inverter to maintain a steady-state velocity. As both HAM and FEM are implemented in the same computer with Intel Core i7-4770@3.40 GHz and 32 GB RAM, it is feasible to compare their computational efficiency by recording the computing time.

A. Magnetic Field

Figs. 10–11 show the predicted magnetic field using SCM, HAM, and 2D-FEM under open-circuit condition and maximum load condition, respectively. Both SCM and HAM predictions agree well with 2D-FEM results under open-circuit condition due to negligible iron saturation. SCM significantly overestimates the y component of air-gap flux density at maximum load compared with the nonlinear 2D-FEM calculation, but it agrees well with the infinite 2D-FEM result, as shown in Figs. 11(b). As

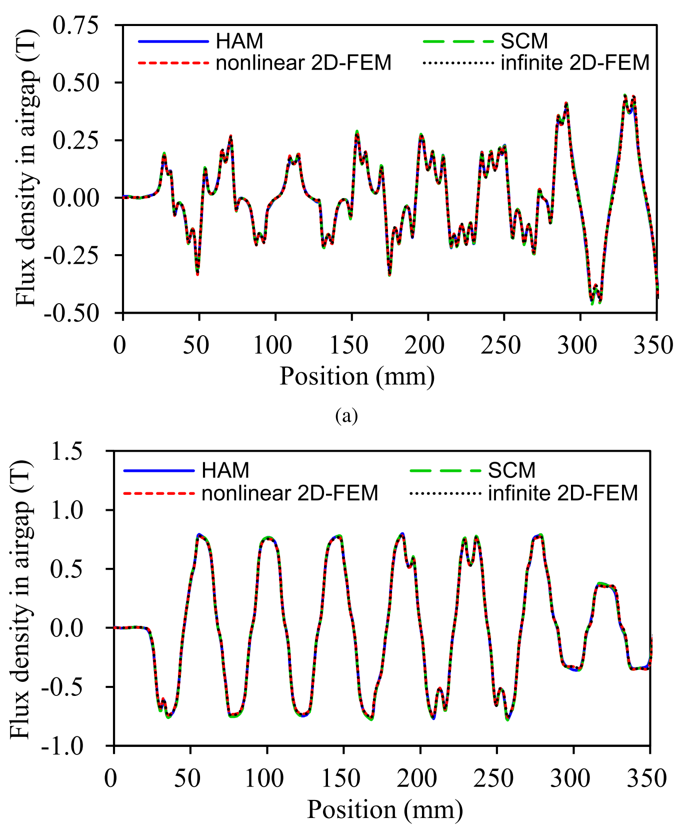

(a)

(b)

Fig. 10. Air-gap field distribution of PMLM under open-circuit condition. (a) X-axis component. (b) Y-axis component.

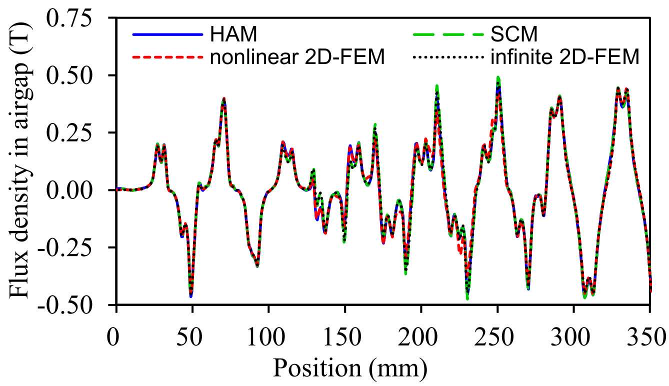

(a)

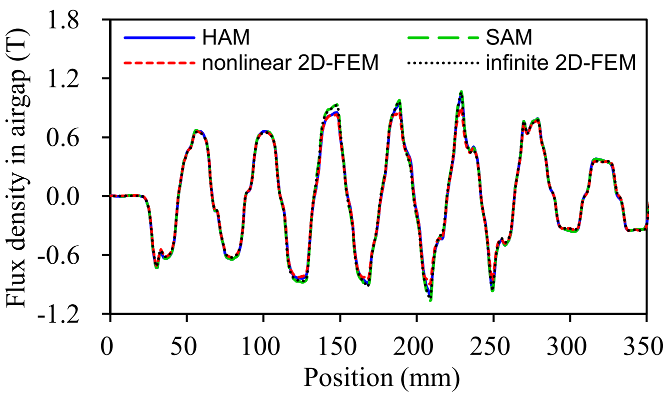

(b)

Fig. 11. Air-gap field distribution of PMLM at maximum load. (a) X-axis component. (b) Y-axis component.

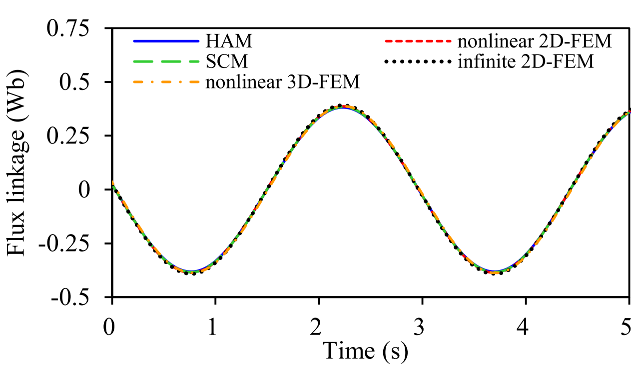

Fig. 12. Open-circuit flux linkage of PMLM.

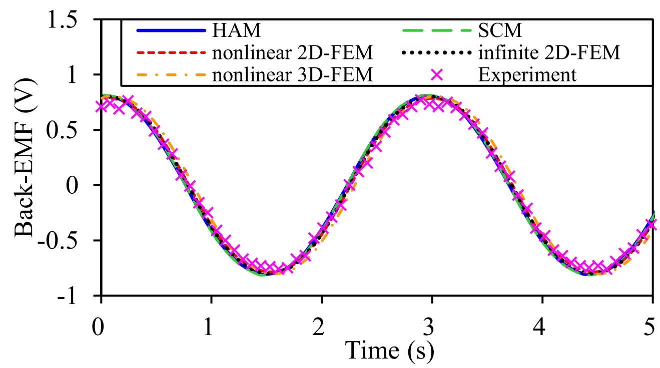

Fig. 13. Open-circuit back-EMF of PMLM at 0.015 m/s.

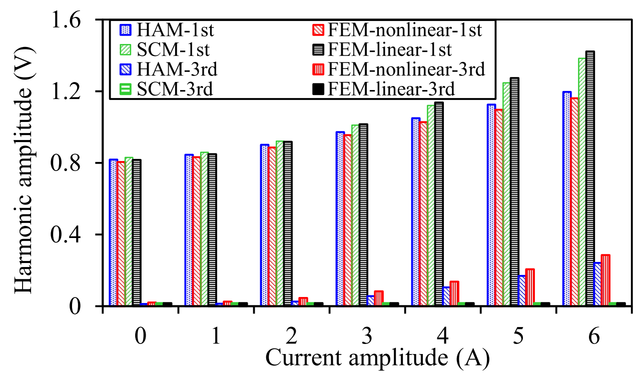

(a)

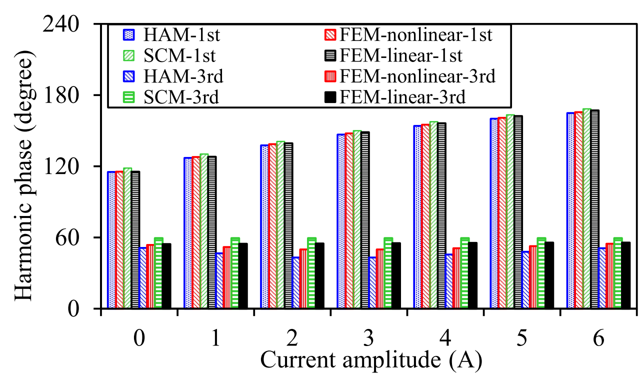

(b)

Fig. 14. Relationship between the harmonic voltage and current amplitude at 0.015 m/s. (a) Amplitude. (b) Phase.

for HAM, it shows great accuracy at maximum load, especially where there is significant saturation in the primary iron.

B. Flux Linkage and back-EMF

Figs. 12–13 show high accuracy of open-circuit flux linkage and back-EMF predictions using either SCM or HAM when compared with nonlinear 2D-FEM and 3D-FEM. The back-EMF of the prototype was measured at 0.015 m/s from the initial position. The errors of predicted back-EMF amplitude using SCM, HAM, and nonlinear 2D-FEM are 5.8%, 4.6%, and 2.6%, respectively. In Fig. 14, the induced voltage of PMLM is predicted at different currents to account for iron saturation. Large errors of the fundamental and the third-order harmonic amplitudes are observed for SCM and infinite 2D-FEM due to neglecting iron saturation while HAM predictions agree well with nonlinear 2D-FEM. As for the harmonic voltage phase, the fundamental harmonic phase using HAM shows better accuracy than the third-order harmonic phase due to the simplification of iron region using the modified MCM. Besides, the accuracy of the third-order harmonic phase for SCM and infinite 2D-FEM can be neglected as their corresponding amplitudes are too small.

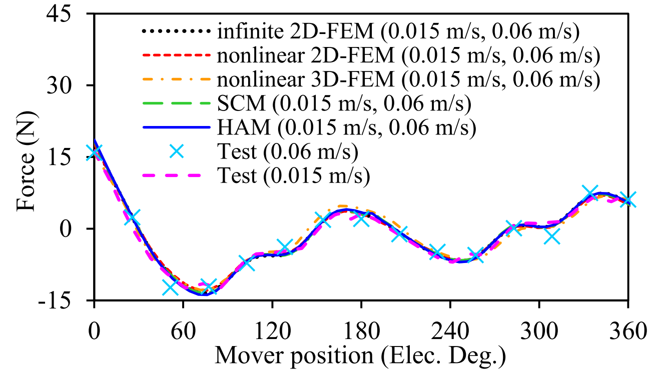

(a)

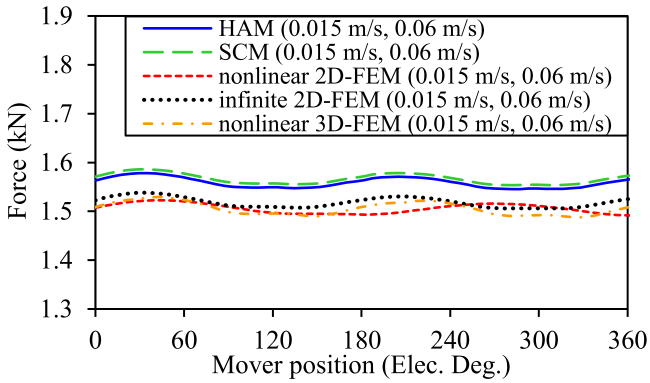

(b)

Fig. 15. Force waveform of PMLM under open-circuit condition. (a) Thrust force. (b) Normal force.

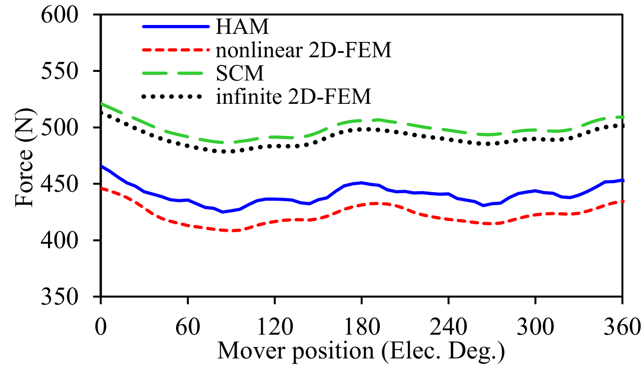

(a)

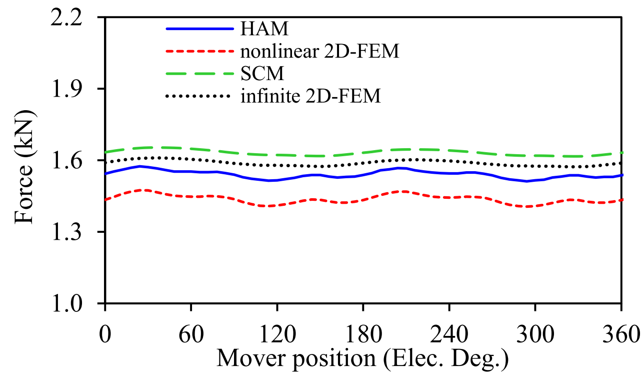

(b)

Fig. 16. Force waveform of PMLM at maximum load and 0.015 m/s. (a) Thrust force. (b) Normal force.

TABLE II
CALCULATION TIME OF HAM AND 2D-FEM

Current (A)	nonlinear 2D-FEM (min)	HAM (min)	infinite 2D-FEM (min)	SCM (min)
0	14.6	2.5	10.2	0.5
1	14.5	2.6	10.4	0.6
2	14.6	2.8	10.5	0.5
3	14.8	3.3	10.5	0.5
4	14.8	3.7	10.6	0.6
5	15.0	3.8	10.7	0.6
6	15.1	4.2	10.6	0.6

C. *Thrust Force and Normal Force*

The thrust force and normal force of the PMLM at different load conditions are predicted using SCM, HAM, 2D-FEM, and 3D-FEM. The initial position of PMLM is shown in Fig. 7. SCM and HAM predictions are compared with the FEM and test results, as shown in Figs. 15–17. Compared with the measurement, the waveforms of the thrust force prediction using SCM, HAM, and FEM under open-circuit condition all show excellent accuracy in Fig. 15(a), which account for the end effect. SCM, HAM, and FEM exhibit the same force values at different speed while the measured thrust force at 0.015 m/s and 0.06 m/s agrees well with each other, as shown in Fig. 15. It demonstrates that the speed of PMLM has negligible influence on the dynamic end effect. For the normal force of the PMLM in Fig. 15(b), the average errors of both analytical models are less than 3.6% compared with 2D-FEM calculations, due to the negligible influence of iron saturation under open-circuit condition.

For the largest thrust force waveform in Fig. 16(a), both HAM and 2D-FEM present similar waveforms, but the HAM has slightly larger values than 2D-FEM due to the oversimplified magnetic circuit in the iron when it is highly saturated. The error of the largest thrust force using HAM is 4.2%. Similarly, the error of the normal force using HAM in Fig. 16(b) is 7.2%, which is a bit large, but it represents the influence of iron saturation on the normal force. Fig. 17 shows the relationship between the force and input current and illustrates that it will introduce large errors if the iron saturation is neglected in the analytical model. The HAM shows high accuracy for thrust force even at the largest load due to considering iron saturation, Fig. 17(a). As for the normal force, even though both analytical models are slightly higher than the FEM calculations, the HAM can accurately exhibit the trend of normal force variation with the increasing current while SCM gives the incorrect prediction due to neglecting iron saturation, Fig. 17(b).

D. *Calculation Time*

The comparison of calculation time between SCM, HAM and 2D-FEM is given in Table II. The time steps within two electrical periods in predicting PMLM performance are 120. The number

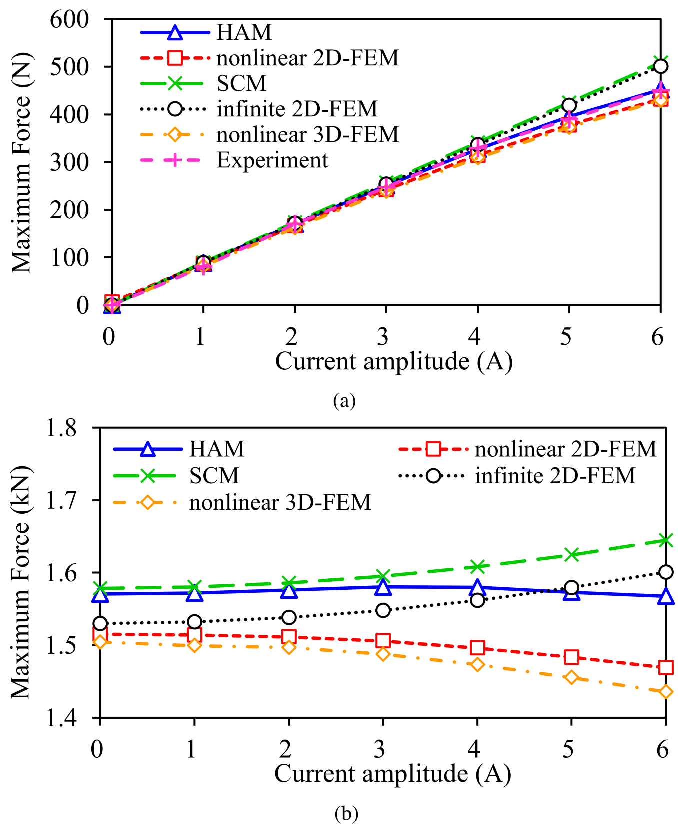

Fig. 17. Relationship between the force and current amplitude at 0.015 m/s. (a) Thrust force. (b) Normal force.

of mesh nodes in the nonlinear 2D-FEM analysis is 186754, while the number of nodes in the magnetic circuit of HAM is 389. The number of node for SCM is 0, as it assumes infinite iron permeability and no magnetic circuits are used. According to Table II, the solving speed using HAM in the platform of MATLAB is over four times as fast as that using 2D-FEM in the platform of Ansys Electronics for the same PMLM. The SCM shows higher computational accuracy than HAM, as it does not require the iteration process to determine the magnetic potential of iron for predicting the air-gap field in the PMLM.

VI. Conclusion

This paper proposed the HAM for predicting the performance of the PMLM with high calculation accuracy and computational efficiency. The SCM is introduced to divide the slotted domain of PMLM into the single end-slot domain and the single mid-slot domain, which significantly improves the computational efficiency. Then, the equivalent saturation current is proposed using the modified magnetic circuit to transform the SCM into the HAM, which improves the prediction accuracy. A prototype of the PMLM is tested to verify the effectiveness of the proposed analytical models. The proposed model demonstrates effectiveness for all the surface-mounted permanent magnet motors with different slot pole combinations and magnetization patterns, regardless of specific design parameters. It can also be extended to analyze double-sided PMLM with short primary or secondary.

References

[1] I. Boldea, L. N. Tutelea, W. Xu, and M. Pucci, “Linear electric machines, drives, and MAGLEVs: An overview,” *IEEE Trans. Ind. Electron.*, vol. 65, no. 9, pp. 7504–7515, Sep. 2018.

[2] Q. Lu, Y. Shen, and Y. Ye, “Development of permanent magnet linear synchronous motors structure and research,” *Proc. CSEE*, vol. 39, no. 09, pp. 2575–2588, May 2019.

[3] Y. Shen and Q. Lu, “Overview of permanent magnet linear machines with primary excitation,” *Trans. China Electrotechnical Soc.*, vol. 36, no. 11, pp. 2325–2343, Jun. 2021.

[4] Y. Shen, Q. Lu, H. Li, J. Cai, X. Huang, and Y. Fang, “Analysis of a novel double-sided yokeless multitooth linear switched-flux pm motor,” *IEEE Trans. Ind. Electron.*, vol. 65, no. 2, pp. 1837–1845, Feb. 2018.

[5] Y. Zhou, R. Qu, D. Li, Y. Gao, and C. H. T. Lee, “Performance investigation and improvement of linear vernier permanent magnet motor for servo application,” *IEEE/ASME Trans. Mechatron.*, vol. 28, no. 5, pp. 2657–2669, Oct. 2023.

[6] Y. Shen, Q. Lu, and Y. Li, “Design criterion and analysis of hybrid-excited vernier reluctance linear machine with slot halbach pm arrays,” *IEEE Trans. Ind. Electron.*, vol. 70, no. 5, pp. 5074–5084, May 2023.

[7] Y. Shen, Z. Zeng, Q. Lu, and C. H. T. Lee, “Design and analysis of double-sided flux concentrated permanent magnet linear machine with saturation relieving effect,” *IEEE Trans. Ind. Electron.*, vol. 70, no. 10, pp. 10442–10453, Oct. 2023.

[8] A. Rahideh, A. Ghaffari, A. Barzegar, and A. Mahmoudi, “Analytical model of slotless brushless pm linear motors considering different magnetization patterns,” *IEEE Trans. Energy Convers.*, vol. 33, no. 4, pp. 1797–1804, Dec. 2018.

[9] Q. Lu, B. Wu, Y. Yao, Y. Shen, and Q. Jiang, “Analytical model of permanent magnet linear synchronous machines considering end effect and slotting effect,” *IEEE Trans. Energy Convers.*, vol. 35, no. 1, pp. 139–148, Mar. 2020.

[10] B. L. J. Gysen, E. A. Lomonova, J. J. H. Paulides, and A. J. A. Vandenput, “Analytical and numerical techniques for solving laplace and poisson equations in a tubular permanent magnet actuator: Part II Schwarz mapping,” *IEEE Trans. Magn.*, vol. 44, no. 7, pp. 1761–1767, Jul. 2008.

[11] D. C. J. Krop, E. A. Lomonova, and A. J. A. Vandenput, “Application of Schwarz-Christoffel mapping to permanent-magnet linear motor analysis,” *IEEE Trans. Magn.*, vol. 44, no. 3, pp. 352–359, Mar. 2008.

[12] S. G. Min and B. Sarlioglu, “Analytical prediction and multiconstrained nonlinear optimization of slotted linear pm motors taking into account two-dimensional end effects,” *IEEE Trans. Ind. Electron.*, vol. 67, no. 4, pp. 2965–2976, Apr. 2020.

[13] H. Hu, J. Zhao, X. Liu, Y. Guo, and J. Zhu, “No-load magnetic field and cogging force calculation in linear permanent-magnet synchronous machines with semiclosed slots,” *IEEE Trans. Ind. Electron.*, vol. 64, no. 7, pp. 5564–5575, Jul. 2017.

[14] Y. Zhao, Y. Li, and Q. Lu, “An accurate no-load analytical model of flat linear permanent magnet synchronous machine accounting for end effects,” *IEEE Trans. Magn.*, vol. 59, no. 1, pp. 1–11, Jan. 2023.

[15] F. Chen, C. Zhang, J. Chen, and G. Yang, “Accurate subdomain model for computing magnetic field of short moving-magnet linear motor with halbach array,” *IEEE Trans. Magn.*, vol. 56, no. 9, pp. 1–9, Sep. 2020.

[16] W. Wang, M. Cheng, X. Li, M. Tong, and J. Qi, “Nonlinear analytical solution of magnetic field and performances of a spoke array vernier permanent magnet machine,” *IEEE Trans. Energy Convers.*, vol. 36, no. 1, pp. 173–185, Mar. 2021.

[17] C. Sun, Y. Fang, and P.-D. Pfister, “Comparison of two finite-permeability subdomain models for surface-mounted permanent-magnet machines,” *IEEE Access*, vol. 11, pp. 73470–73477, 2023.

[18] E. Kazan and A. Onat, “Modeling of air core permanent-magnet linear motors with a simplified nonlinear magnetic analysis,” *IEEE Trans. Magn.*, vol. 47, no. 6, pp. 1753–1762, Jun. 2011.

[19] G. Liu, L. Ding, W. Zhao, Q. Chen, and S. Jiang, “Nonlinear equivalent magnetic network of a linear permanent magnet vernier machine with end effect consideration,” *IEEE Trans. Magn.*, vol. 54, no. 1, pp. 1–9, Jan. 2018.

[20] Y. Laoubi, M. Dhifli, G. Verez, Y. Amara, and G. Barakat, “Open circuit performance analysis of a permanent magnet linear machine using a new hybrid analytical model,” *IEEE Trans. Magn.*, vol. 51, no. 3, pp. 1–4, Mar. 2015.

[21] L. Wu, H. Yin, D. Wang, and Y. Fang, “On-load field prediction in SPM machines by a subdomain and magnetic circuit hybrid model,” *IEEE Trans. Ind. Electron.*, vol. 67, no. 9, pp. 7190–7201, 2020.

[22] Z. Li, X. Huang, J. Ma, Z. Chen, A. Liu, and L. Peretti, "Hybrid analytical model for predicting the electromagnetic losses in surface-mounted permanent-magnet motors," *IEEE Trans. Transp. Electrific.*, early access, doi: 10.1109/TTE.2023.3289869.

[23] Z. Li, Z. Chen, Y. Shen, Y. Ma, X. Huang, and L. Peretti, "Analytical analysis of quasi-halbach array permanent-magnet motors based on field separation theory," *IEEE Trans. Transp. Electrific.*, early access, doi: 10.1109/TTE.2023.3300968.

[24] Z. Li et al., "An improved hybrid field model for calculating on-load performance of interior permanent-magnet motors," *IEEE Trans. Ind. Electron.*, vol. 68, no. 10, pp. 9207–9217, Oct. 2021.

[25] Z. Li, X. Huang, L. Wu, T. Long, B. Shi, and H. Zhang, "Open-circuit field prediction of interior permanent-magnet motor using hybrid field model accounting for saturation," *IEEE Trans. Magn.*, vol. 55, no. 7, pp. 1–7, Jul. 2019.

[26] Z. Li, X. Huang, Z. Chen, L. Wu, Y. Shen, and T. Shi, "Electromagnetic analysis for interior permanent-magnet machine using hybrid subdomain model," *IEEE Trans. Energy Convers.*, vol. 37, no. 2, pp. 1223–1232, Jun. 2022.

[27] Z. Li, X. Huang, A. Liu, Z. Liu, L. Wu, and T. Shi, "Analytical model of electromagnetic performance for permanent-magnet vernier machines using nonlinear exact conformal model," *IEEE Trans. Transp. Electrific.*, vol. 8, no. 2, pp. 2005–2014, Jun. 2022.

[28] T. C. O'Connell and P. T. Krein, "A Schwarzchristoffel-based analytical method for electric machine field analysis," *IEEE Trans. Energy Convers.*, vol. 24, no. 3, pp. 565–577, Sep. 2009.

[29] B. Hague, *The Principles of Electromagnetism Applied to Electrical Machines*. Mineola, NY, USA: Dover, 1962.

[30] W. Ullah, F. Khan, S. Hussain, M. Yousuf, and S. Akbar, "Analytical modeling of novel high thrust force density segmented pm consequent pole linear flux switching machine," *IEEE Access*, vol. 10, pp. 105887–105897, 2022.

[31] M. Wang, L. Li, and D. Pan, "Detent force compensation for PMLSM systems based on structural design and control method combination," *IEEE Trans. Ind. Electron.*, vol. 62, no. 11, pp. 6845–6854, Nov. 2015.

[32] Y. Zhu, G. Liu, L. Xu, W. Zhao, and D. Cao, "A hybrid analytical model for permanent magnet Vernier machines considering saturation effect," *IEEE Trans. Ind. Electron.*, vol. 69, no. 2, pp. 1211–1223, Feb. 2022.

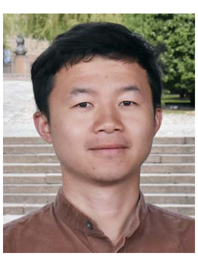

Zhaokai Li (Member, IEEE) received the B.S. and Ph.D. degrees in electrical engineering from Zhejiang University, Hangzhou, China, in 2015 and 2020, respectively. From 2018 to 2019, he was a Visiting Student with the University of Cambridge, Cambridge, U.K. From 2020 to 2022, he was a Postdoctoral Researcher with Zhejiang University. He then continued the Postdoctoral Research with KTH Royal Institute of Technology, Stockholm, Sweden. From 2023, he was a Guest Researcher with ABB Corporate Research, Váster's, Sweden. His research interests include analytical models and iron loss analysis for permanent magnet motors.

Lize Wu (Graduate Student Member, IEEE) received the B.Eng. degree in electrical engineering in 2021 from Zhejiang University, Hangzhou, China, where she is currently working toward the Ph.D. degree with the College of Electrical Engineering. Her research interests include optimal design and analysis of linear permanent magnet machines.

Yanxin Li (Member, IEEE) received the B.Eng. and M.Eng. degrees in electrical engineering from Zhejiang University, Hangzhou, China, in 2011 and 2014, respectively, and the Ph.D. degree from the University of Sheffield, Sheffield, U.K., in 2018. Since 2020, he has been a Tenure-tracked Associate Professor with the Zhejiang University. His research interests include the modeling, design, and analysis of linear machine.

Qinfen Lu (Senior Member, IEEE) received the B.Eng., M.Sc., and Ph.D. degrees from Zhejiang University, Hangzhou, China, in 1996, 1999, and 2005, respectively, all in electrical engineering. Since 1999, she has been with the College of Electrical Engineering, Zhejiang University, where she is currently a Professor. Her research interests include analysis and control of linear machines and permanent-magnet machines.

Xiaoyan Huang (Member, IEEE) received the B.E. degree in control measurement techniques and instrumentation from Zhejiang University, Hangzhou, China, in 2003, and the Ph.D. degree in electrical machines and drives from the University of Nottingham, Nottingham, U.K., in 2008. From 2008 to 2009, she was a Research Fellow with the University of Nottingham. She is currently a Professor with the College of Electrical Engineering, Zhejiang University. Her research interests include PM machines and drives for aerospace and traction applications, and generator system for urban networks.

Luca Peretti (Senior Member, IEEE) was born in 1980. He received the M.Sc. degree from the University of Udine, Udine, Italy, in 2005, and the Ph.D. degree from the University of Padova, Padua, Italy, in 2009. Between 2010 and 2018, he was with ABB Corporate Research, Váster's, Sweden. He then joined the KTH Royal Institute of Technology, Stockholm, Sweden, as Associate Professor. His research interests include (multiphase) machines and drives, their control, and diagnostics, for industrial, renewable, and automotive applications.

Yiming Shen (Member, IEEE) received the B.Eng. and Ph.D. degrees in electrical engineering from the College of Electrical Engineering, Zhejiang University, Hangzhou, China, in 2015 and 2020, respectively. He is currently a Research Fellow with the School of Electrical and Electronic Engineering, Nanyang Technological University, Singapore. His research interests include design and analysis of novel permanent magnet machines with particular reference to linear machines for direct drive applications.